Determining the Porosity of Polypyrrole Membranes for use in Potassium Air Batteries

Undergraduate Honors Thesis

Presented in Partial Fulfillment of the Requirements for Graduation with Distinction in the Department of Mechanical and Aerospace Engineering at The Ohio State University

by

Thomas Ziebro

Undergraduate Program in the Department of Mechanical and Aerospace Engineering

The Ohio State University

April 2016

Thesis Committee:

Advisor: Vishnu Baba Sundaresan, Ph.D.

Vishwanath Subramaniam, Ph.D.

Abstract

One of the biggest limitations in the implementation of renewable energies is a lack in the ability to store large quantities of electricity efficiently. One promising technology is the metal-air battery, which offers the potential for high electrochemical energy storage capacity that exceeds that of comparable metal ion batteries. Of the metal-air batteries, the potassium-air system has one of the fastest, one-electron redox processes. Currently, the fundamental limitation of potassium-air batteries is the crossover of molecular oxygen from the cathode to potassium anode, leading to the formation of potassium superoxide on the anode surface. This process reduces the availability of the metal participating in energy storage, and causes self-discharge. One solution to this problem is the introduction of a functionally graded conducting polymer membrane into the cathode to isolate the chemical reaction and minimize molecular oxygen crossover to the anode. Critical metrics to cathode construction are maximal ionic conductivity, but minimal air porosity.

The objective of this research is to obtain air porosity values for membrane materials used in the battery separator to understand oxygen transport across the cathode. To do so, a novel testing apparatus was developed with the capability to measure airflow impedance. This information is intended towards design of the cathodes for world's first reliable potassium-air battery.

Dedication

This thesis is dedicated to my parents, Richard J. and Elsie M. Ziebro; to my brothers, John M. and Mark J. Ziebro; and in memory of my grandmother, Eleanor V. Roe, who lives on in my sense of curiosity and adventure.

Acknowledgements

I would like to thank the National Science Foundation for providing the funding to make this project a reality. I would also like to thank the Ohio State University College of Engineering for awarding me with the Undergraduate Research Scholarship for the 2015-2016 school year.

I would also like to express my sincere gratitude to my advisor, Dr. Vishnu Baba Sundaresan, for his unwavering support and encouragement. I want to thank all of my colleagues in the Integrated Material Systems Laboratory for their friendliness and patience, especially Paul Gilmore and Dr. Robert Northcutt, who have always been willing to lend a hand with my problems, no matter how insurmountable I felt they were.

Finally, I would like to thank my family and friends for their encouragement and understanding. I feel very fortunate to have had the opportunity to conduct research as an undergraduate student, and hope to pursue my enthusiasm throughout graduate school.

Table of Contents

Abstract iii

Dedication iv

Acknowledgements v

Table of Contents vi

List of Figures viii

List of Tables x

Chapter 1: Motivation 11

Introduction 11

Types of Batteries 13

Limitations on Current Battery Technology 16

Solution to Molecular Oxygen Crossover 18

Conducting Polymers 19

Chapter 2: Design of Experiment 21

Objective 21

Design of Measurement Apparatus 21

Design of Electronics and Instrumentation 24

Design Stage Uncertainty 28

Chapter 3: Experiments 30

Fabrication of Substrates and Fabrication of Membrane 30

Experimental Procedure 32

Adjustments to Experimental Setup....33

Data....36

Statistical Significance....37

Chapter 4: Conclusions....40

Summary of Scientific Contributions....40

Recommendation for Continuation and Further Improvements of this Work....41

References....42

Appendix A: Sample Calculation....44

Appendix B: MATLAB Code....45

Appendix C: Instrument Specification Sheets....50

List of Figures

Figure 1: Ragone plot indicating the relative specific power and specific energy of batteries 12

Figure 2: Voltage curve of K-O_2 battery for first charge-discharge cycle (Ren, 2013) 15

Figure 3: Voltage curve of Li-O_2 battery for first charge-discharge cycle (Ren, 2013) 16

Figure 4: Current K-Air battery construction (Gilmore, 2016) 18

Figure 5: Proposed modifications to the air battery (Gilmore, 2016) 19

Figure 6: Representation of flow through porous media 21

Figure 7: Prototype testing apparatus used for collecting data. From left to right: membrane fixture, CTA, CTA fixture, pressure transducer, fan adapter, and fan. 23

Figure 8: Electrical schematic of measurement instrumentation 25

Figure 9: Front view of experimental setup 25

Figure 10: Top view of experimental setup 26

Figure 11: Instrumentation block diagram 26

Figure 12: Simulink model used to run experiment 27

Figure 13: Materials tested, including (A) carbon substrate, (B) polypropylene, (C) polypropylene + gold, and (D) polypropylene + gold + polypyrrole (300 nC/cm^2) 31

Figure 14: Max pressure calibration 33

Figure 15: Zero pressure calibration 33

Figure 16: Modified membrane fixture design 35

Figure 17: Aluminum backflow shielding plate 35

Figure 18: Simplified experimental apparatus (with new nozzle, with backflow shield, and without CTA retaining mechanism) 36

Figure 19: Manifold pressure for each membrane in the ionic separator 36

Figure 20: Data sorted into histogram bins and fit to a normal probability density function for pressure data using the total composite membrane....38

Figure 21: Pressure transducer specification sheet....51

Figure 22: Operational amplifier specification sheet....52

Figure 23: dSpace data acquisition specifications....53

List of Tables

Table 1: Overview of battery technologies (Ren, 2013) 14

Table 2: Analysis of the contamination layer of the potassium anode (Ren, 2014) 17

Table 3: Methods for polypyrrole fabrication (Sasso, 2011) 20

Table 4: Summary of electrical components 24

Table 7: Uncertainty specifications with total uncertainty propagation 29

Table 5: Experimental Results 37

Table 6: Summary of statistical analysis 39

Chapter 1: Motivation

Introduction

There has never been a time of greater concern for energy-related issues as today. The search for a more diversified renewable energy portfolio is a subject of necessity for many political leaders, economists, and scientists alike. Wind, solar, hydroelectric, and biomass sources are currently being investigated as potential solutions to the world's energy crisis. However, there are many factors that inhibit the implementation of this advanced technology. Cost, material availability, intermittency, and energy density are all parameters that must be considered when evaluating the efficacy of renewable energy sources.

From a technical perspective, the concerns of both energy density and intermittency can be addressed with the implementation of high efficiency, high capacity energy storage devices. There are several types of storage devices, each with multifaceted advantages and disadvantages. They can be grouped roughly into four categories: capacitors, supercapacitors, batteries, and fuel cells. For this discussion, a Ragone plot is helpful in characterizing various devices with respect to energy density and specific energy (as seen in Figure 1).

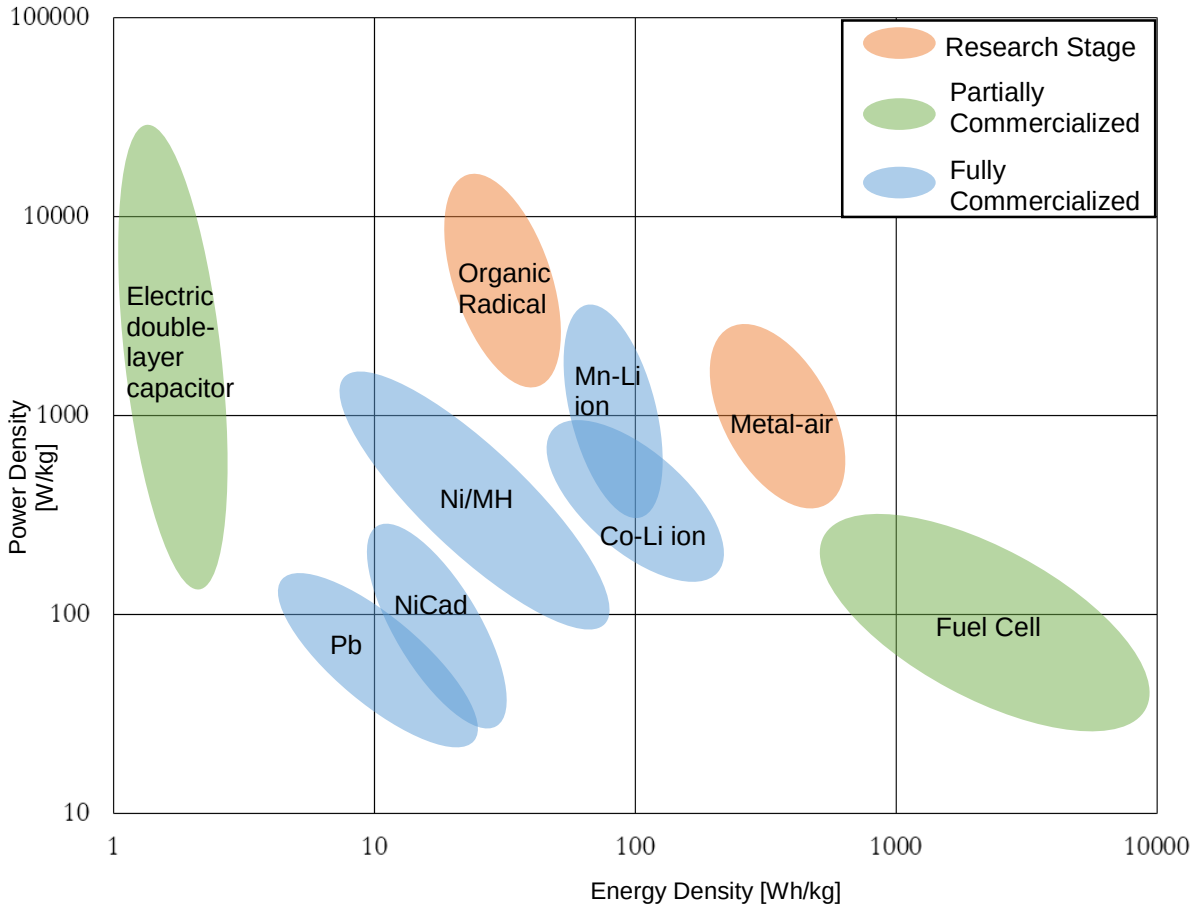

Figure 1: Ragone plot indicating the relative specific power and specific energy of batteries

The Ragone plot exhibits two extreme cases, one with higher specific power and low specific energy, and one with lower specific power and high specific energy. High specific energy and low specific power materials, such as fuel cells, are able to store large amounts of energy but have very slow charge-discharge rates. This is in contrast to capacitors, which can dissipate energy extremely rapidly, but cannot store large enough amounts for practical use. In the middle are supercapacitors and batteries, which have moderate specific energy and specific power. The reason for the differences is the physical method by which charge is stored. For capacitors and supercapacitors, the charge carrier is an electron, which can move close to the speed of light. However, it can be difficult to pack electrons close enough together to safely achieve a substantial amount of charge. Because of how

small and fast electrons are, it is difficult to research and develop new technologies for electron entrapment. For fuel cells, the charge carriers are chemical bonds, which involve large amounts of energy to break and form. Since this process of forming and breaking apart chemical bonds can be time-consuming, catalysts and activators need to be researched in more depth before fuel cell systems can be economical.

With batteries, chemical ions carry charge from the anode to the cathode. Unlike the previous two systems (capacitors and supercapacitors or fuel cells), chemical ions are conveniently large enough to manipulate, and are not too large that ion transport cannot occur sufficiently quickly. Thus, the focus of this research focuses on improving the efficiency of battery technology.

Types of Batteries

Currently, there are several types of batteries commercially available, with varying energy densities, efficiencies, and costs as seen in Table 1. Traditionally, electrolytic batteries operate via ion transport through an electrolyte and some separator membrane with pore size dependent on the materials used. In more recent years, much simpler batteries have been developed that use gaseous oxygen from the atmosphere and aqueous metal ions as charge carriers, instead of two aqueous ions. Called metal-air batteries, these devices are much lighter and can store more energy than conventional batteries.

Table 1: Overview of battery technologies (Ren, 2013)

Technologies	Energy Density (Wh/kg)	Round-Trip Efficiency (%)	Cost ($/kWh)	Comments
Lead-acid	30-45	75-80	100-150	Toxic elements used
Sodium-sulfur	150-240	75	450-550	High working temperature (300°C)
Lithium-ion	100-150	85-95	500-800	Limited Li resources
Zn-O_2	220-340	75	350	High cost catalysts; in development
Li-O_2	290-315	60	500	Limited Li resources
K-O_2	310	Up to 98	89	In development

The K-O_2 row in Table 1 refers to a recent discovery by a research team at The Ohio State University Department of Chemistry. This team has discovered that potassium superoxide batteries are a much more realistic electrolytic reaction than that of any of the other electrochemical battery to use in storage systems. They are more thermodynamically stable, more commercially available, and less environmentally toxic than lithium oxide batteries. This is because battery chemistries like those of lithium-air are asymmetrical. The following two reactions happen simultaneously in a lithium air battery.

$$2Li^+ + 2e^- + O_2 \leftrightarrow Li_2O_2 \quad (1)$$

$$4Li^+ + 4e^- + O_2 \leftrightarrow 2Li_2O \quad (2)$$

This is in contrast to the potassium-air battery's chemistry, which is symmetric.

$$O_2 + e^- + K^+ \leftrightarrow KO_2 \quad (3)$$

By taking advantage of the reversibility of the O_2 / O_2^- redox couple, the research group found that a charge/discharge potential gap of less than 50 mV is possible with the potassium-air configuration (Ren, 2013). This is in contrast to lithium air batteries, which tend to have a much larger potential gap develop over time. Another factor that contributes to this phenomenon is the high charge density of Li^+ making LiO_2 unstable. The potential gap of a potassium-air cell and a similarly constructed lithium air cell can be seen in Figures 2 and 3.

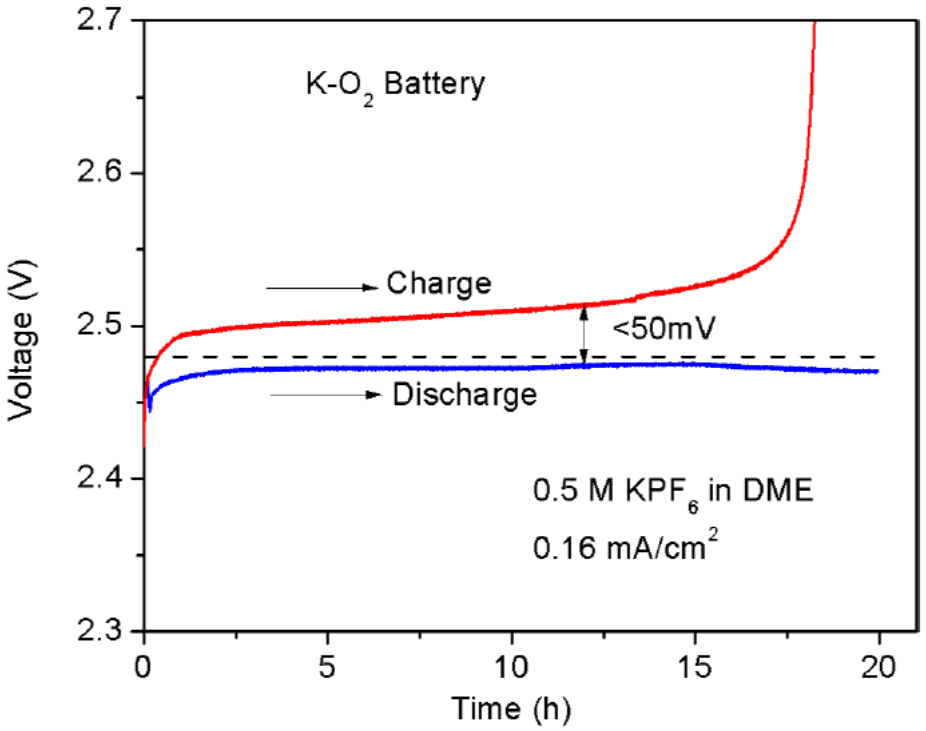

Figure 2: Voltage curve of K-O_2 battery for first charge-discharge cycle (Ren, 2013)

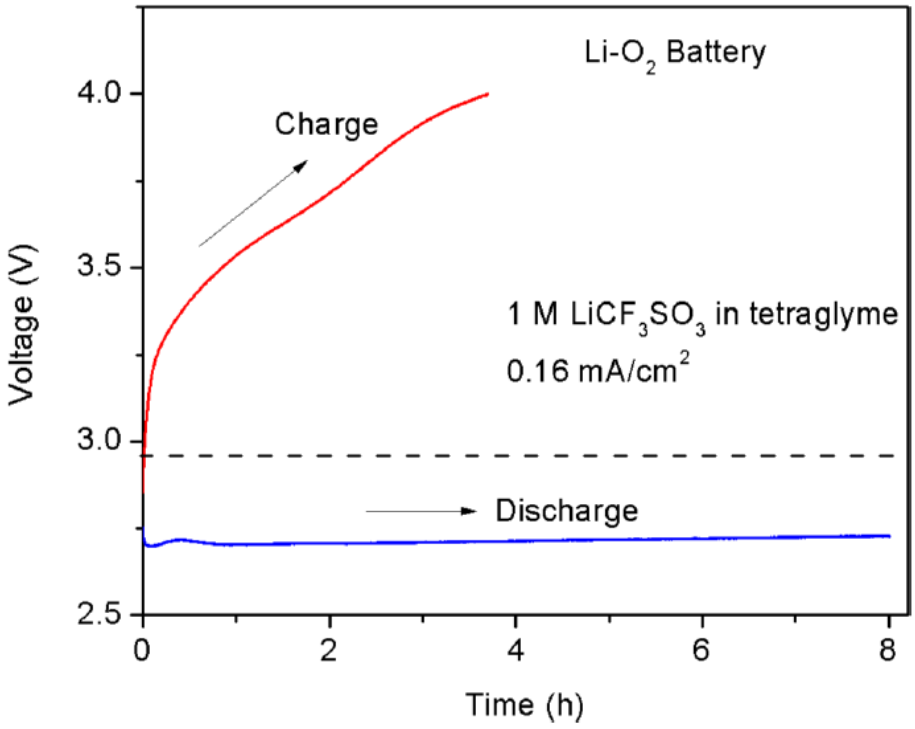

Figure 3: Voltage curve of Li-O_2 battery for first charge-discharge cycle (Ren, 2013)

It can be seen from these two plots, that the potassium air battery exhibits much more stable behavior, from 0 to 15 hours, than the lithium air configuration does during its entire operation lifetime.

Limitations on Current Battery Technology

There are several factors that inhibit the efficiency of battery operation over time. Such examples include thermal effects, membrane degradation, and contamination. The focus of this research was on the contamination problem. Like all metal-air batteries, the alkali metal (in this case, potassium) within the battery is highly reactive, so much that it reacts with any contaminants that may be present in the cathode. In conventional lithium-ion batteries, this layer is known as the solid

electrolyte interface, or SEI. In the case of lithium-ion batteries, the SEI has been shown to stabilize the anode, but it appears that the surface layer on potassium anodes due to side reactions will result in suppressed ion transport. The same laboratory that pioneered the potassium air battery also conducted testing for contaminant formed on the potassium metal surface.

This measurement was collected by modifying Nafion-H^+ membranes to Nafion-K^+ by submersion and heating in a potassium hydroxide solution. After drying, the membrane was sandwiched between two class fiber separators, and submerged into the electrolyte, 0.5 M KPF_6 in 1,2-dimethoxyethane. After the cell was conditioned, attenuated total reflectance infrared spectroscopies (ATR-IR) were employed to characterize the main components in the surface layer. The following table summarizes the findings.

Table 2: Analysis of the contamination layer of the potassium anode (Ren, 2014)

	weight percentage (%)				
	after cycle tests			after discharge	
	A	B	C	D	E
KO_2	22.2	20.5	22.1	27.2	26.1
KPF_6	10.7	9.7	12.9	13.4	15.4
KOH	44.3	48.0	42.9	41.2	39.5
K_2CO_3	5.2	6.0	8.0	5.9	6.3
organic side products	2.6	2.7	3.9	4.3	5.0
sum	85.0	86.9	89.8	92.0	92.3

While the mechanics of electrolytic potassium ion transport are still being researched, it is clear that the crossover of O_2 molecules from the cathode to the anode pose an eminent threat to the efficiency and the lifetime of the potassium-air battery. As seen in the above table, potassium superoxide constitutes 22% of the contamination layer on the potassium metal. Thus, one solution is the integration of an interior layer into the battery that would both allow potassium ions to freely

flow through the electrolyte, while at the same time preventing molecular oxygen from permeating into the battery and ultimately the anodic metal.

Solution to Molecular Oxygen Crossover

One solution to oxygen crossover in K-O2 batteries that the Integrated Material Systems Laboratory proposes is to introduce a conducting polymer layer as a sieve. As previously discussed, this material would need to be highly ionically conductive (10^{-3} – 10^{-1} S/cm) with low oxygen permeability. This material would be placed nearest to the outside of the battery, with porosity ranging from high to low from outside to inside, respectively. A symbolic representation of the current battery configuration during discharging can be seem in Figure 4.

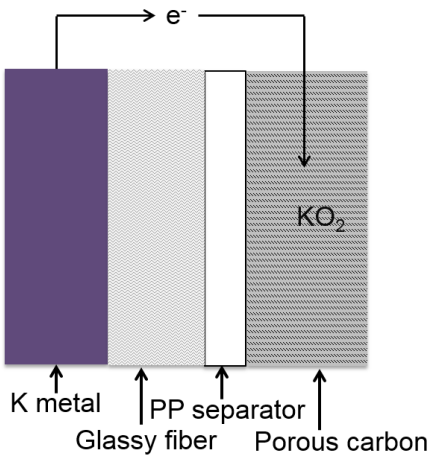

Figure 4: Current K-Air battery construction (Gilmore, 2016)

During the charging process, potassium ions are driven toward the potassium metal from the porous carbon cathode via an applied potential. As a result of the oxygen evolution reaction of potassium superoxide, molecular oxygen is released into the ambient environment. When discharging, the potassium ions are driven away from the potassium metal and form potassium superoxide with molecular oxygen from the ambient environment. This uncontrolled introduction of molecular

oxygen into the battery results in transport across the polypropylene separator, and the eventual formation of potassium superoxide on the surface of the anode. To prevent this phenomenon, a proposed modification would take the form of the following:

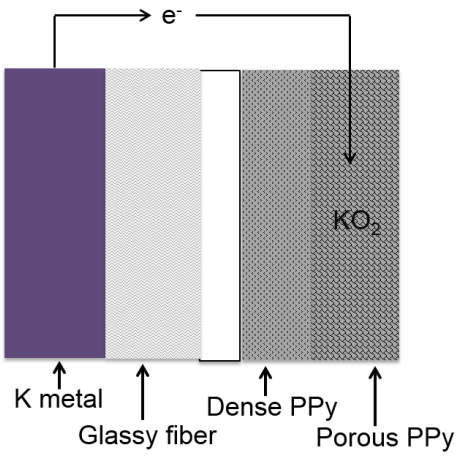

Figure 5: Proposed modifications to the air battery (Gilmore, 2016)

In this system, PPy refers to a specific type of conducting polymer known as polypyrrole, which is an ideal material for applications involving ion transport. This is because the material can be highly conducive to ion transport, while at the same time having a functionally graded porosity to molecular oxygen, where the most porous region is located on the outermost area of the battery, and the less porous region is located further inside the battery. Please see the following section for a more detailed background on PPy.

Conducting Polymers

Conducting polymers are organic, electrically conductive, and are highly customizable morphologically. There are several different types of conducting polymers, each with their unique characteristics. For this research, sodium dodecylbenzenesulfonate (NaDBS) was selected as a

dopant, and Polypyrrole (PPy) was chosen based on the combination's compatibility with the transport of electrolytic ions in KPF_6.

The process by which polypyrrole is polymerized can be accomplished in several ways. These are described in Table 3, below.

Table 3: Methods for polypyrrole fabrication (Sasso, 2011)

Synthesis	Type	Conductivity (max) S/cm	Mechanical properties	High-volume production
Electrochemical	PPy films	+++ (10^3)	- - -	- -
	Py electropolymerisation on preformed plastic film	++ (50)	+	- -
Chemical	Soluble/dispersible PPy	+ (5)	++	-
	PPy/insulating polymer composites by compression moulding	++ (10)	++	++
	PPy/insulating polymer composites by mixing	+ (1)	++	+++

Since electrochemical synthesis of PPy films tends to yield higher conductivities, the PPy used in this experiment will be formed by electropolymerization. In the context of this research, critical metrics that need to be satisfied with the dense PPy are low oxygen permeability and high ionic conductivity, while the porous PPy needs to have high electrical conductivity as well, but porous enough to allow oxygen diffusion to the surface and store insoluble discharge compounds.

Research has been conducted to characterize the ionic properties of conducting polymers, especially the properties of polypyrrole as they relate to its ability to act as an actuator (Northcutt and Sundaresan, 2015). However, for the specific application of metal-air batteries, there is little data on how conducting polymers might affect fluid impedance on the total separator overall.

Chapter 2: Design of Experiment

Objective

The primary objective of this research is to quantify the air fluidic permeability of membranes used as separators in potassium-air batteries. In order to accomplish this objective, a novel experimental setup was designed and constructed with representative data collected.

Design of Measurement Apparatus

Before any prototypes were made, it was essential to identify the physical goals of the project. For simplicity, oxygen permeability was interpreted as a fluid impedance, which is effectively the ratio of pressure difference to the resultant flow. In classical system dynamics, this can be represented as a throttling valve.

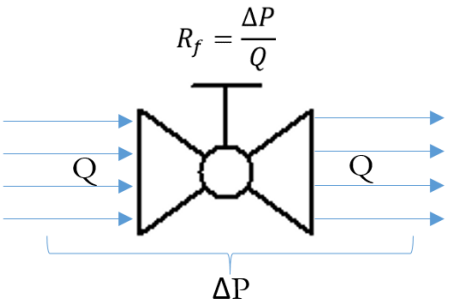

Figure 6: Representation of flow through porous media

Where R_f is the fluid impedance to flow, Q is the volumetric flow rate, and ΔP is the pressure difference on either side of the valve.

Unfortunately, the membrane does not behave exactly like a linearized throttling valve. For the linearization to remain valid, the linearization point must be selected such that the real world deviation from that point is minimal. Thus, for this experiment, it was critical to test the membrane

at pressures and flows that were representative of the application. Since these batteries were not designed to be pressurized from pure oxygen, and are open to atmospheric pressure, it would be prudent to assume low operating pressure (<10 Pa gauge pressure) and flows proportional to charge time. Faster charge/discharge processes would produce faster flow rates, whereas slower battery operation would produce the opposite.

There needed to be a way to create a pressure difference across the membrane via stagnation pressure. While it would be simple to pressurize some vessel, block a hole with a membrane, and test the resultant flow, this would not be similar enough to represent the application. Such a test is known as the Gurley method, whereby an apparatus measures the amount of time it takes for a fixed volume of gas to be forced through a membrane at constant pressure. However, most of these methods involve relatively high pressures, and since the battery is naturally aspirated, it was required to create a stagnation pressure via airflow. Because the battery is currently designed to operate on the timescale of minutes and hours, it was assumed that flow from a 12VDC computer fan would provide enough airflow to measure manifold pressure with enough resolution. This pressure would be measured with a sensitive pressure transducer, and a CTA would measure the resultant airflow passing through the membrane.

The experiment needed to

- Be airtight
- Protect a delicate CTA
- Be cost-effective
- Provide as much flow as possible, for highest pressure resolution
- Establish a flow in chamber
- Be easily and quickly assembled and modified

In order to minimize flow losses from sharp inside corners, it was decided to make the entire structure cylindrical. This would minimize vortices within the flow, which could potentially cause noisy pressure fields which are unrelated to the experiment.

Material was obtained, and adaptors were 3D printed using fused deposition modeling (FDM). A CTA fixturing device was designed to accurately raise and lower the measuring device, without harming the sensitive thermoelectric wire. 1/8" dowel pins with pen springs were used to automatically retract the CTA when needed. a circular collar was attached to this fixture to fasten it to the pipe. The fan adaptor design was relatively straightforward, since the contour of the fan mandated screw holes. The membrane clamping mechanism needed much more complex geometry, because the internal geometry needed to taper down to a smaller area than the outside, which needed to taper into a flat surface. The membrane was secured via four screws, and a hole was made on the ambient side of the membrane for the CTA to measure the airflow velocity along the centerline of the cylinder.

After several design iterations, the following apparatus was constructed.

Figure 7: Prototype testing apparatus used for collecting data. From left to right: membrane fixture, CTA, CTA fixture, pressure transducer, fan adapter, and fan.

Design of Electronics and Instrumentation

The sensitivity of the sensors used to collect data was very important in this experiment for two reasons. First, the pressure difference between the inside of the chamber and ambient was expected to be extremely small (<10 Pa). Second, if there were to be a laminar flow, it would be important to measure the difference in fluid velocity from the centerline to the boundary. Electrical components are summarized below.

Table 4: Summary of electrical components

Manufacturer / #	Description	Input Voltage	Output Voltage
Dantec Dynamics / 54T42-9054N0802	Constant Temperature Anemometer	+12VDC, GND	0V – 5V
Mineba Co. / 3110KL-04W-B20	DC Fan	+12VDC, GND	
Burr-Brown / INA114	Operational Amplifier	+12VDC, -12VDC, GND	-12V – 12V
Omega Engineering / PXCPC-004WCGV	Pressure Transducer	+12VDC, GND	0 mV – 25 mV
dSpace Gmbh. / DS1104	dSpace	-10 VDC – 10 VDC	
Mastech / HY3005F-3	Power Supply	120 VAC, 60 Hz	+12 VDC, GND, -12 VDC

Combining the electrical components was relatively simple. Figure 8 provides an electrical schematic of how each instrument was implemented.

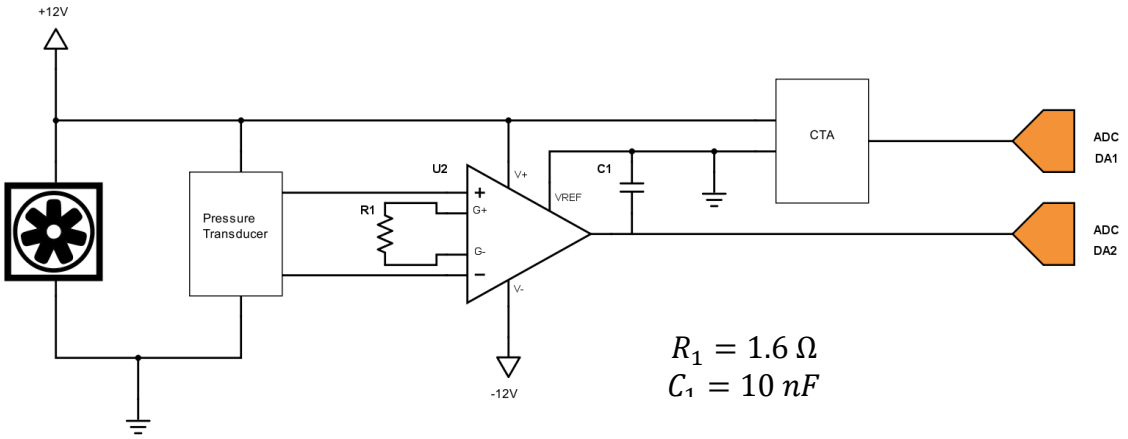

Figure 8: Electrical schematic of measurement instrumentation

Figures 9 and 10 portray the experimental setup.

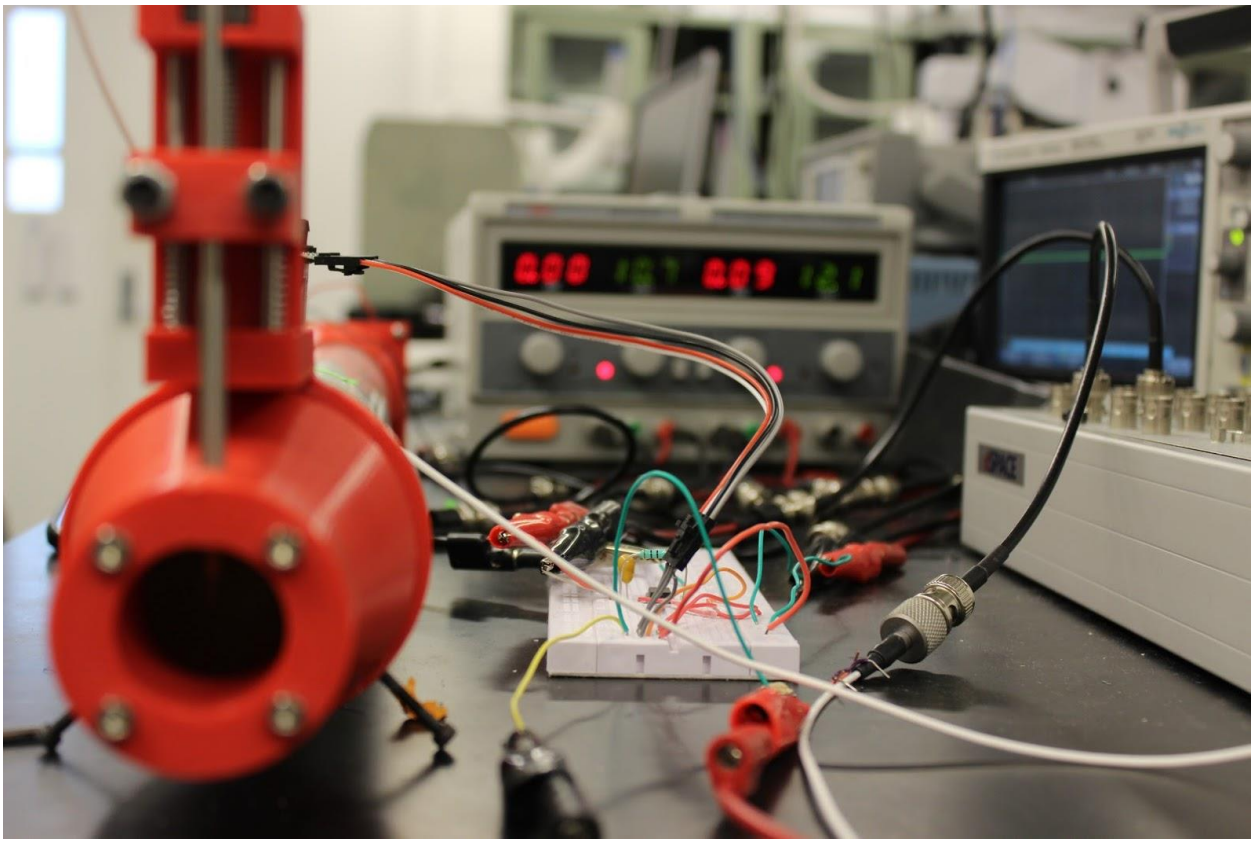

Figure 9: Front view of experimental setup

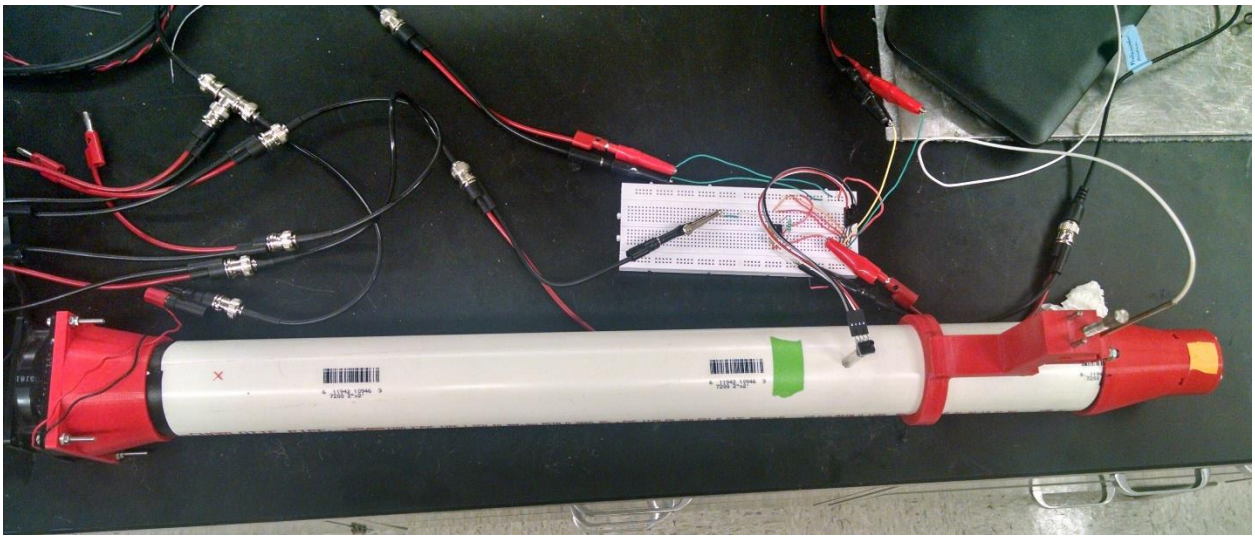

Figure 10: Top view of experimental setup

Figure 11, below, is a block diagram that summarizes the dataflow of the experiment.

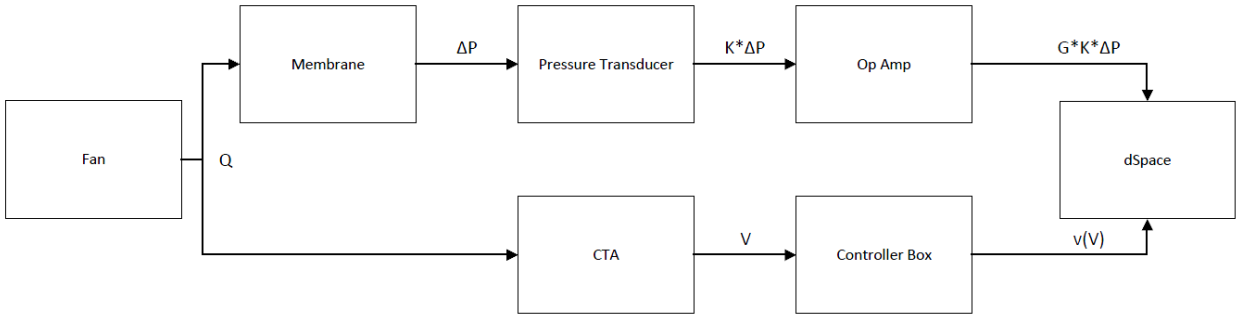

Figure 11: Instrumentation block diagram

In this figure, it is necessary to understand the static sensitivity of the pressure transducer, K, the op amp gain, G, and finally, the calibration function that allows the transformation from CTA voltage to velocity. According to the specification sheet, the pressure transducer can output a maximum of 25 mV at a pressure of 4 in. of H_2O.

$$K = \frac{\partial \mathrm{V}}{\partial \Delta P} = \frac{25\ mV}{4\ in\ H_2O} \times \frac{1\ in\ H_2O}{249.1\ Pa} \times \frac{1\ V}{1000\ mV} = 2.509 \times 10^{-5}\ \frac{V}{Pa} \quad (4)$$

$$G = \frac{\partial V}{\partial V} = 1 + \frac{50\ k\Omega}{R_1} = 1 + \frac{50000\ \Omega}{1.6\ \Omega} = 3.125 \times 10^4 \quad (5)$$

Note that since the maximum gain is 10,000 on the op amp, this figure was used for calculations. Once these sensitivities were calculated, dSpace was modified to compile Simulink files. Figure 12, below, shows the Simulink model used to run this experiment. Note that the gain of 10 is a function of the hardware, and that the Simulink model simply assigns a data acquisition channel to a recordable variable. A time step of 0.0005 seconds was used because data was only recorded for 10 seconds, which is not an unreasonably long time. Since the Simulink solver step size feeds directly into the dSpace sampling rate, a time step of 0.005 seconds corresponds to 200 Hz.

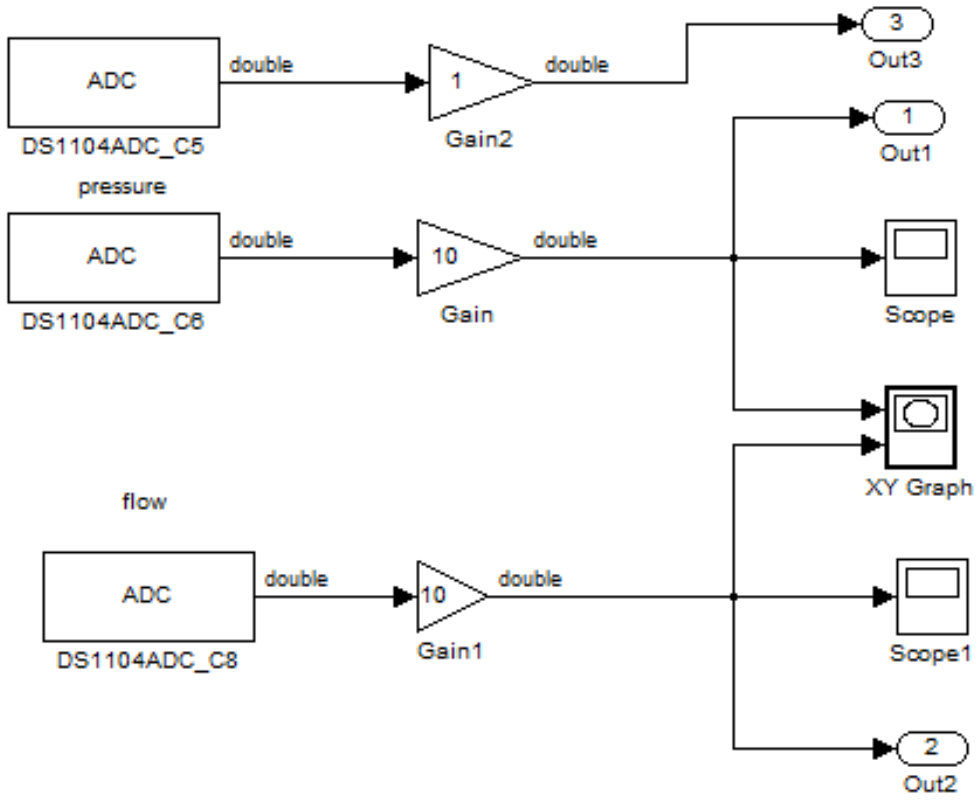

Figure 12: Simulink model used to run experiment

Design Stage Uncertainty

In order to assess the validity of this experiment, one needs some metric that takes into account all of the uncertainties with each component. For this discussion, the root-sum-squares method of uncertainty propagation can be used.

$$u_x = \sqrt{u_1^2 + u_2^2 + \cdots + u_k^2} \tag{6}$$

For pressure transducer (offset + linearity error):

$$u_{pt} = \sqrt{(1\ mV)^2 + (0.01)^2(25\ mV)^2} = 1.03\ mV \tag{7}$$

For ADC (quantization error for 12-bit ADC):

$$u_{ADC} = \sqrt{\frac{\left(\frac{1}{2}\right)(FSR)}{2^N}} = \sqrt{\frac{(0.5)^2(10000)^2}{(2^{12})^2}} = 1.22\ mV \tag{8}$$

For op amp (gain error + linearity error):

$$u_{OA} = \sqrt{(0.01)^2(25\ mV)^2 + (0.0001)^2(27400\ mV)^2} = 2.75\ mV \tag{9}$$

For total system (dividing by gain from op amp)

$$u_{total} = \left(2.509 \times 10^{-2}\frac{mV}{Pa}\right)^{-1}\left(10000\frac{mV}{mV}\right)^{-1}\sqrt{(1.03\ mV)^2 + (1.22\ mV)^2 + (2.75\ mV)^2} \tag{10}$$

$$= 0.0127\ Pa$$

It can be seen that the most uncertainty comes from the op amp. However, when compared to the results expected, a total pressure uncertainty of 0.01 Pa is less than 5% of the measured values. Table 7 on the following page formally presents the uncertainty information.

Table 5: Uncertainty specifications with total uncertainty propagation

Source	**Uncertainty**
Transducer Offset	±1 mV
Transducer Linearity Error	1% FSR = ±0.25 mV
Op Amp Gain Error	0.01% of Gain = ±1 mV
Op Amp Linearity Error	1% FSR = ±0.25 mV
12-bit ADC Quantization Error	± 2.44 mV
Resultant Pressure Uncertainty	± 0.0127 Pa
Resultant Flow Uncertainty	$\pm 4.607 \cdot 10^{-6}$ m^3/s

Chapter 3: Experiments

Fabrication of Substrates and Fabrication of Membrane

While this research did not specifically focus on electropolymerization, it is important to understand how polypyrrole is synthesized, so that one has some intuition as to how the material will function. As mentioned previously, polypyrrole is a conducting polymer with highly customizable morphology (Northcutt, 2015).

Polypyrrole for this research is produced electrochemically, via electropolymerization with a three-electrode configuration. A working electrode, counter electrode, and reference electrode are electrochemically connected through an electropolymerization solution consisting of the monomer (pyrrole) and a dopant salt (sodium dodecylbenzenesulfonate – NaDBS) at prescribed concentrations. The working electrode and counter electrode are highly conductive, chemically inert metals. In this instance Ag/AgCl was used as a reference electrode and gold foil was used as a counter electrode.

In this research, four membranes were tested: (1) typical carbon paper, which is common to the battery community; (2) polypropylene, which serves as the base layer; (3) polypropylene with 25 nm of gold sputtered onto the surface; and (4) polypropylene with 25 nm of sputtered gold and a layer of electropolymerized PPy(DBS) with a charge density of 300 mC/cm^2.

Pictures of these materials can be found on the next page, in Figure 13.

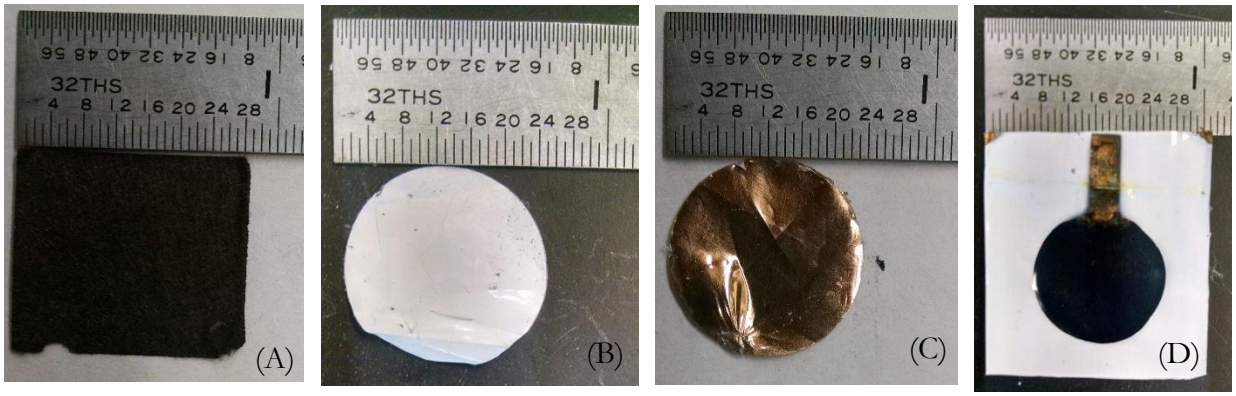

Figure 13: Materials tested, including (A) carbon substrate, (B) polypropylene, (C) polypropylene + gold, and (D) polypropylene + gold + polypyrrole (300 mC/cm^2)

Experimental Procedure

The steps taken to collect data on this experimental setup were as follows:

1. The power supply was turned on, MATLAB/Simulink was opened, and a new build was initiated via dSpace. The layout file was loaded, as well as the variable files. Both channels were checked to make sure the hardware was functional (i.e. the user blew on the CTA, or gently tapped on the pressure transducer.
2. Data was collected for the case with no membrane loaded, with the fan off. Both channels of data were saved.
3. Data was collected for the case with a finger blocking the only flow path (besides back flowing against the fan). This served as a maximal manifold pressure measurement. If any measurement thereafter exceeded this pressure, then the experiment needed to be restarted.
4. Data was collected for the case with no membrane loaded, but with the fan on. Both channels of the data were saved. Before each trial, the power supply was carefully set to 12 V and monitored to ensure that the supplied voltage stayed exactly at 12 V. If there was any change in the provided voltage, another trial replaced that data.
5. Data was collected twice for each of the materials: (1) the carbon substrate, (2) polypropylene, (3) polypropylene with sputtered gold, and (4) polypropylene with sputtered gold and polypyrrole.
6. Between each set, data was collected for the open case. This was to account for any change in atmospheric pressure or other outside parameter that may have occurred during the experiment.

Adjustments to Experimental Setup

After conducting several experiments, it was discovered that the calibration curve for the CTA was poorly sensitive to low airflow velocities. After evaluating the raw voltage output from the sensor controller with the fourth-order calibration polynomial, a negative flow velocity results. This was because the CTA was only rated accurate in flow velocities above 5 m/s. Because the resolution of the CTA was far too low and the resolution of the pressure transducer was relatively high, it was decided to make simplifying assumptions to calculate the airflow rate leaving the system. The following figures illustrate these simplifying assumptions.

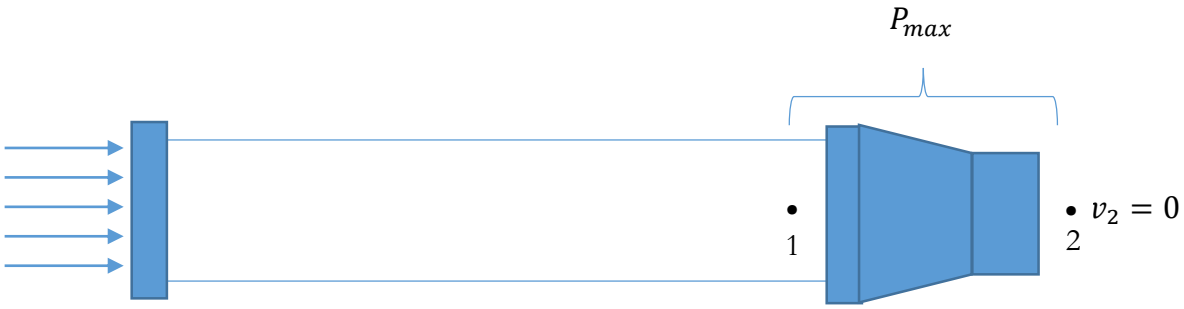

Figure 14: Max pressure calibration

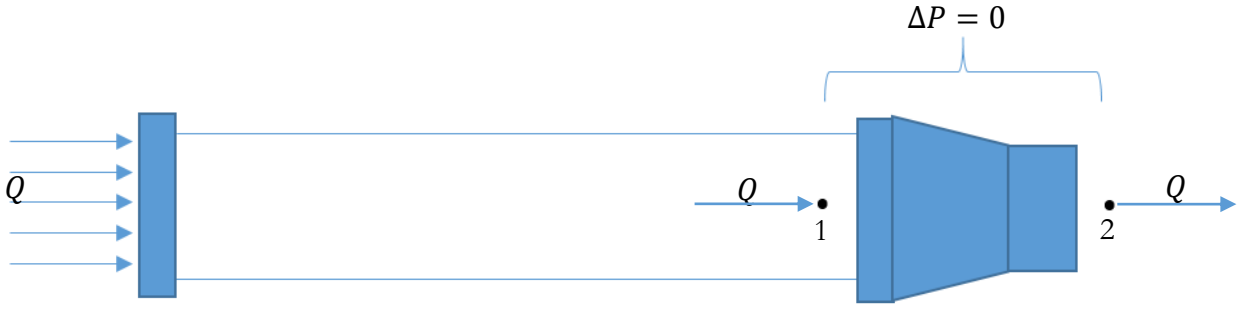

Figure 15: Zero pressure calibration

In order to analyze the system, lumped parameter methods were used. In the first case, the exit was completely blocked. This stagnation pressure was the maximum that could be obtained from the fan. This parameter was called P_{max}.The second case provided a static calibration measurement that could be later subtracted from subsequent measurements. Finally, after installing each membrane into the fixture, a manifold pressure was read, which could be subtracted from the maximal pressure to obtain the energy lost from the system. This idea can be summarized as an energy balance as shown below:

$$P_{max} - P = \frac{1}{2}\rho v_2^2 \tag{11}$$

It can also be rearranged explicitly for velocity:

$$v_2 = \sqrt{\frac{2(P_{max}-P)}{\rho}} \tag{12}$$

And velocity can be used to find volumetric flow rate:

$$Q = A_2 v_2 \tag{13}$$

This enables the calculation of the fluid resistance:

$$R_f = \frac{P_{max}-P}{Q} = \frac{P_{max}-P}{A_2}\sqrt{\frac{\rho}{2(P_{max}-P)}} \tag{14}$$

To maximize the resolution of the pressure transducer and accommodate smaller membranes, the membrane fixturing device was modified to have a smaller exit area. This is pictured in Figure 16, on the following page.

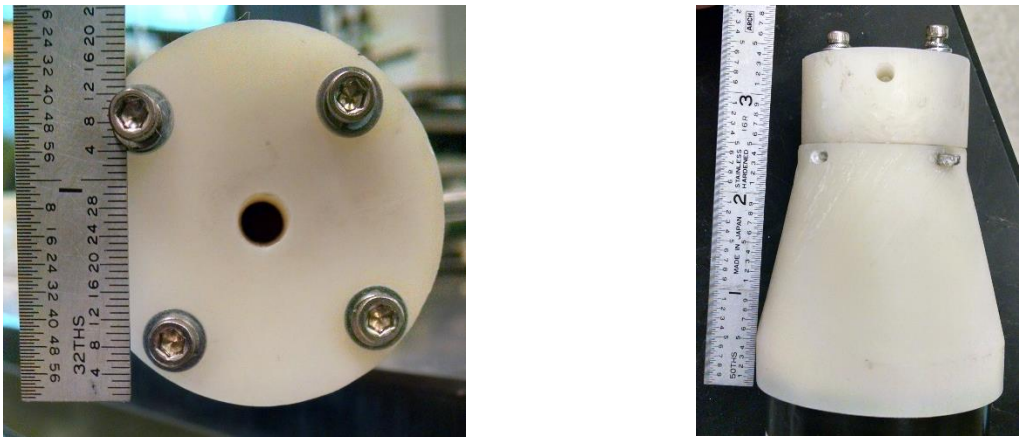

Figure 16: Modified membrane fixture design

Another issue that became apparent after several trials was a large manifold impedance to flow. The root cause of this problem was leakage from the fan. Thus, a plate was fabricated out of aluminum to minimize backflow from the fan. This component is picture below in Figure 17.

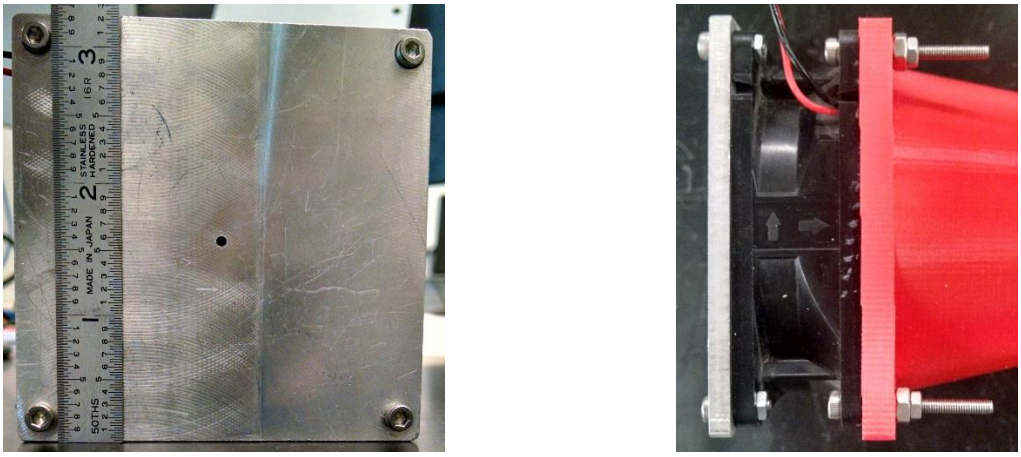

Figure 17: Aluminum backflow shielding plate

For simplicity, the CTA retaining mechanism was removed. The final testing setup can be seen on the following page in Figure 18.

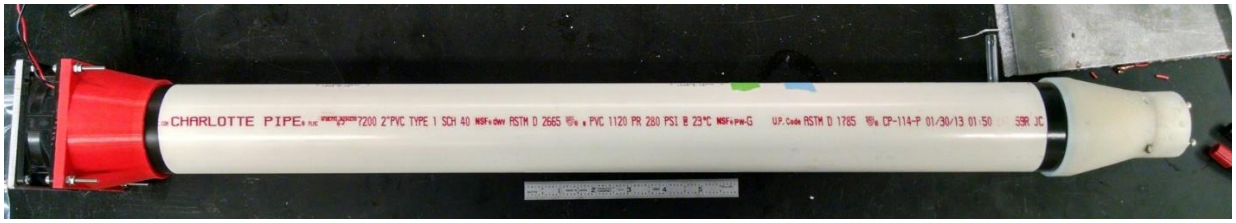

Figure 18: Simplified experimental apparatus (with new nozzle, with backflow shield, and without CTA retaining mechanism)

Data

The manifold pressure for each membrane is plotted on the same graph (Figure 19), and results after calculations are tabulated in Table 5.

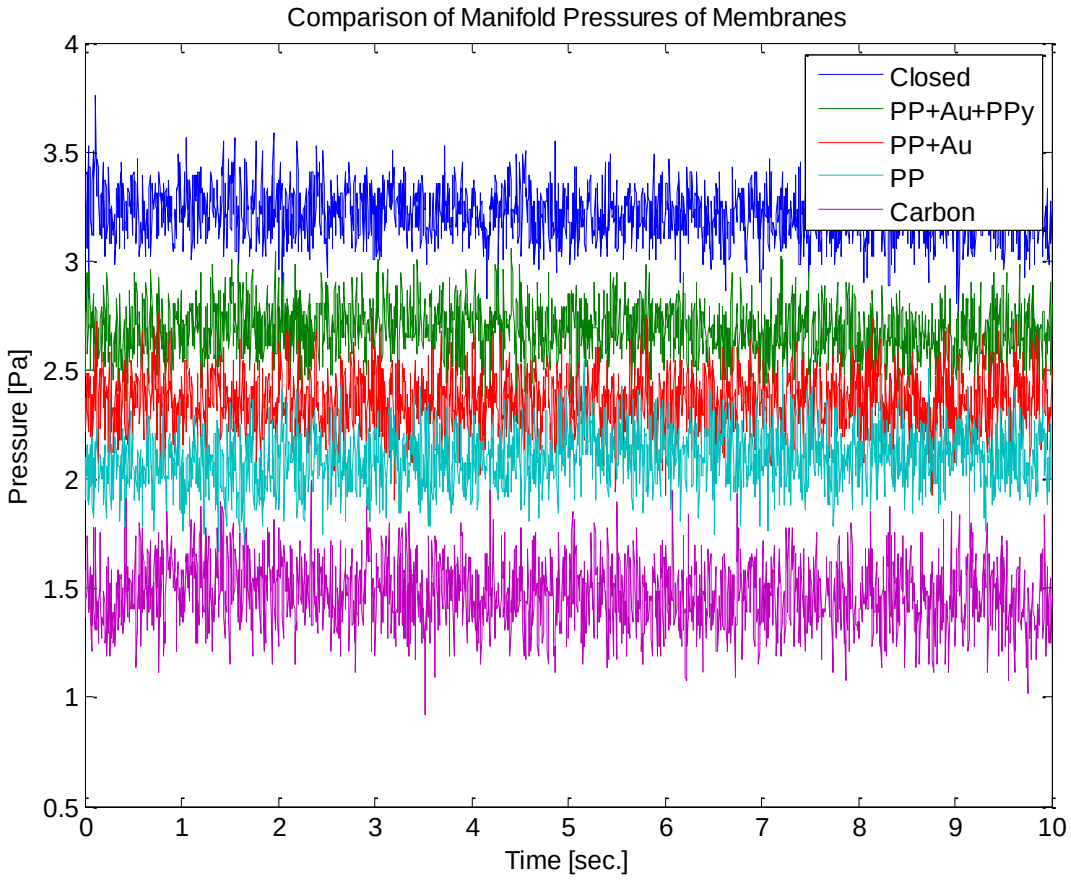

Figure 19: Manifold pressure for each membrane in the ionic separator

Table 6: Experimental Results

Material	**Manifold Pressure [Pa]**	**Velocity [m/s]**	**Flow Rate [m^3/s]**	**Fluid Resistance [Pa*s/m^3]**
Carbon	1.472	1.705	0.54×10^{-6}	27.3×10^{3}
Polypropylene	2.094	1.367	0.43×10^{-6}	48.4×10^{3}
Polypropylene + Gold	2.354	1.198	0.38×10^{-6}	62.1×10^{3}
Polypropylene + Gold + Polypyrrole	2.682	0.943	0.30×10^{-6}	89.8×10^{3}

Statistical Significance

The above data was calculated using average pressure values. To achieve a more complete understanding of how close the sample mean of the pressure data is to the true mean, a standard 95% confidence interval can be calculated. The data can be assumed to follow a normal distribution, as seen in Figure 20.

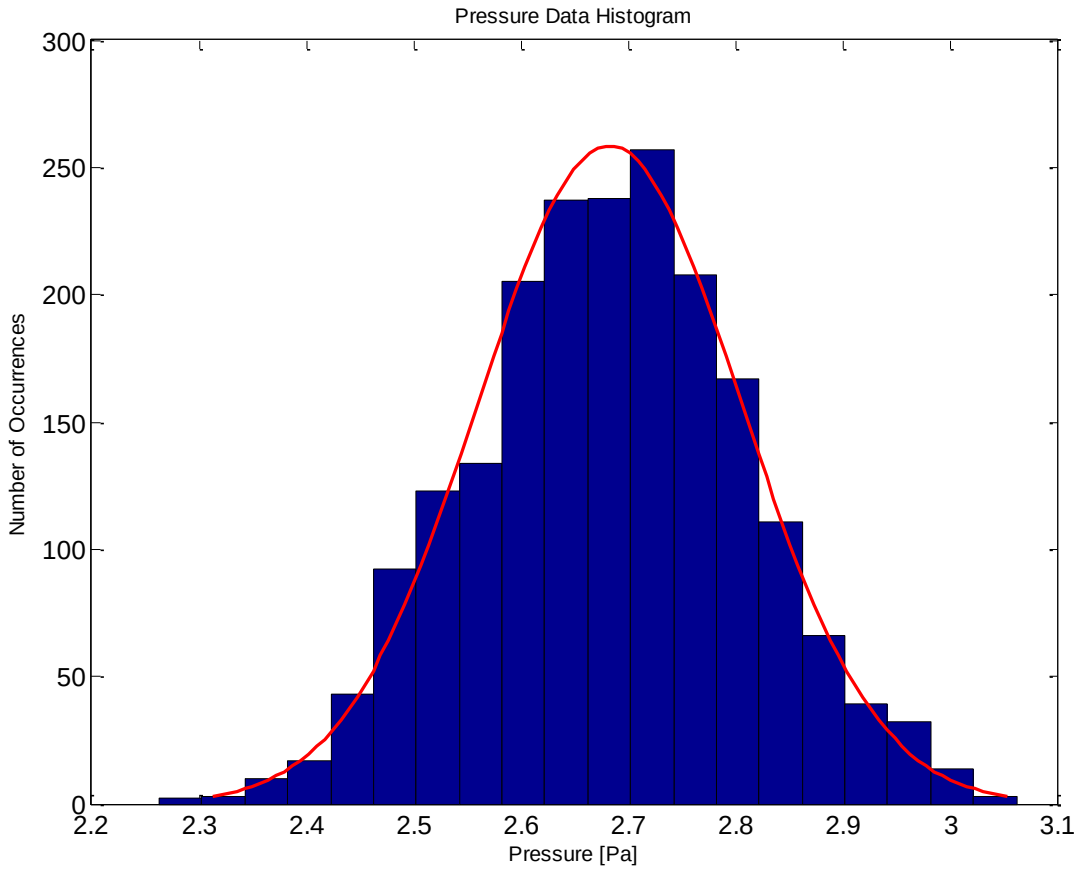

Figure 20: Data sorted into histogram bins and fit to a normal probability density function for pressure data using the total composite membrane

First, the mean pressure was calculated using Equation 15:

$$\bar{x} = \frac{\sum x_i}{N} \tag{15}$$

where x_i is each individual sample, and N is the number of samples. Next, the standard deviation was calculated with Equation 16.

$$s_x = \sqrt{\frac{1}{N-1}\sum_{i=1}^{N}|x_i - \bar{x}|^2} \tag{16}$$

Finally, a cumulative distribution function was used to calculate z^*. The confidence interval was then calculated via Equation 17:

$$CI = \bar{x} \pm \frac{z^* s_x}{\sqrt{N}} \tag{17}$$

A summary of these findings can be found below, in Table 7.

Table 7: Summary of statistical analysis

Material	Avg. Pressure [Pa]	Std. Dev. [Pa]	95% Confidence Interval [Pa]	
Carbon	1.472	0.152	1.466	1.478
Polypropylene	2.094	0.131	2.087	2.101
Polypropylene + Gold	2.354	0.129	2.347	2.362
Polypropylene + Gold + Polypyrrole	2.682	0.123	2.674	2.690

Chapter 4: Conclusions

The objective of this research was to construct an experimental setup to test the resistance of various ionically conductive films to air. This work was completed, and the uncertainty calculation lends credence to the validity of the results. In an experiment where more than 1 Pascal is significant, an uncertainty of less than 0.01 Pascals is sufficient. The results are intuitive: that the more porous a substance is, the less flow will permeate through it, and the higher the manifold pressure and fluid resistance. Since a static calibration was performed before each experiment, it is likely that this canceled out many of the uncertainty terms from above, which adds accuracy and precision.

Summary of Scientific Contributions

- *Design of an experiment to measure membrane porosity to air*

  Using lumped parameter models and design stage uncertainty considerations, a testing apparatus was designed to measure the fluidic impedance of any membrane. This design can be scaled to accommodate both larger membranes and more layers of membranes. All that is needed is a large enough membrane to maintain an airtight fit.

- *Determination of porosity of multiple layers in ionic separator*

  Experimental data was tabulated for each layer in a compound ionic separator. Data from this experiment will be used to determine the best way to construct the total ionic separator, and to identify battery metrics such as operating pressure and membrane thickness. The next experiment will involve measuring ionic permeability in conjunction with air permeability.

- *Possibility of real-time feedback control*

  This device can be used to actively monitor the flow of oxygen into and out of the prototype potassium air battery. This information could then be used to better control the oxygen reduction and oxygen evolution reactions taking place in the cathode to minimize contaminants forming on the anode. This information can also be used to monitor the useful life and reliability of the battery as a function of the ion density captured in the cathode.

Recommendation for Continuation and Further Improvements of this Work

In the future, a more precise CTA should be considered for use in conjunction with the lumped parameter approach. In this way, the fluidic resistance from both cases can be compared and the precision of the data will be improved.

Another improvement to this apparatus would be the introduction of a low-pressure plenum to achieve constant pressure in time. The data collected in this experiment was relatively noisy compared to the average pressure. This device would smooth out these pressure spikes from the fan, and would yield more reliable results.

Finally, if a cross-section of channels were inserted into the pipe, a more laminar flow regime would result, and would further decrease the noise measured by the pressure transducer. This would further increase the precision and accuracy of the results.

References

1. D. D. Ateh, H. A. Navsaria, and P. Vadgama, "Polypyrrole-based conducting polymers and interactions with biological tissues," *Journal of The Royal Society Interface,* vol. 3, pp. 741-752, 2006.
2. P. Gilmore, "Potassium-Air Battery: Group Meeting", Scott Laboratory E525, 17 March 2016.
3. Hruska, "New aluminum air battery could blow past lithium-ion, runs on water | ExtremeTech", ExtremeTech, 2016. [Online]. Available: http://www.extremetech.com/extreme/198462-new-aluminum-air-battery-could-blow-past-lithium-ion-be-refilled-with-water. [Accessed: 04- Apr- 2016].
4. C. O. Laoire, S. Mukerjee, K. M. Abraham, E. J. Plichta, and M. A. Hendrickson, "Elucidating the Mechanism of Oxygen Reduction for Lithium-Air Battery Applications," *The Journal of Physical Chemistry C,* vol. 113, pp. 20127-20134, 2009/11/19 2009.
5. R. Northcutt, "A Mechanistic Interpretation for Charge Storage in Conducting Polymers," Doctor of Philosophy in Mechanical Engineering, Department of Mechanical and Aerospace Engineering, The Ohio State University, Columbus, Ohio, 2015.
6. R. G. Northcutt and V.-B. Sundaresan, "Characterization of Electrochemical Capacity of a Biotemplated Polypyrrole Membrane," presented at the ASME 2013 Conference on Smart Materials, Adaptive Structures, and Intelligent Systems, Snowbird, Utah, USA, 2013.
7. R. Northcutt and V. Sundaresan, "Mechanoelectrochemistry of PPy(DBS) from correlated characterization of electrochemical response and extensional strain", *Phys. Chem. Chem. Phys.*, vol. 17, no. 48, pp. 32268-32275, 2015.
8. M. D. Radin and D. J. Siegel, "Charge transport in lithium peroxide: relevance for rechargeable metal-air batteries," *Energy & Environmental Science,* vol. 6, pp. 2370-2379, 2013.
9. X. Ren, K. C. Lau, M. Yu, X. Bi, E. Kreidler, L. A. Curtiss*, et al.*, "Understanding Side Reactions

in K–O2 Batteries for Improved Cycle Life," *ACS Applied Materials & Interfaces,* vol. 6, pp. 19299-19307, 2014/11/12 2014.

10. X. Ren and Y. Wu, "A Low-Overpotential Potassium–Oxygen Battery Based on Potassium Superoxide," *Journal of the American Chemical Society,* vol. 135, pp. 2923-2926, 2013/02/27 2013.
11. C. Sasso, D. Beneventi, E. Zeno, D. Chaussy, M. Petit-Conil, and N. Belgacem, "Polypyrrole and polypyrrole/wood-derived materials conducting composites: A review," *BioResources,* vol. 6, pp. 3585-3620, 2011.
12. V. B. Sundaresan, S. A. Sarles, and D. J. Leo, "Characterization of porous substrates for biochemical energy conversion devices," 2008, pp. 69280K-69280K-11.
13. V. B. Sundaresan, H. Zhang, R. Northcutt, and S. Salinas, "Dynamics of ion transport in a bio-derived ionic transistor," 2011, pp. 79780B-79780B-11.
14. G. Venugopal, J. Moore, J. Howard, and S. Pendalwar, "Characterization of microporous separators for lithium-ion batteries," *Journal of Power Sources,* vol. 77, pp. 34-41, 1/1/ 1999.
15. V. Venugopal and V. B. Sundaresan, "Polypyrrole-based amperometric cation sensor with tunable sensitivity," *Journal of Intelligent Material Systems and Structures,* September 24, 2015 2015.

Appendix A: Sample Calculation

Fluidic resistance calculation (for carbon substrate):

$$R_f = \frac{P_{max} - P}{A_2}\sqrt{\frac{\rho}{2(P_{max} - P)}} = \frac{(3.2155\ Pa) - (1.4720\ Pa)}{\frac{\pi}{4}\left(0.25in \cdot 0.0254\frac{m}{in}\right)^2}\sqrt{\frac{\left(1.2\frac{kg}{m^3}\right)}{2(3.2155\ Pa - 1.4720\ Pa)}}$$

$$= 27.27 \times 10^3\,\frac{Pa \cdot s}{m^3}$$

Appendix B: MATLAB Code

```
%% Load Data. Note: all pressure transducer data should be inverted
clc;
close all;
clear all;

load('C:\Users\ziebro.2\Dropbox\Interlab Shared
Space\Ziebro_Honors_Thesis\Thesis\c.mat')
load('C:\Users\ziebro.2\Dropbox\Interlab Shared
Space\Ziebro_Honors_Thesis\Thesis\closed2.mat')
load('C:\Users\ziebro.2\Dropbox\Interlab Shared
Space\Ziebro_Honors_Thesis\Thesis\off1.mat')
load('C:\Users\ziebro.2\Dropbox\Interlab Shared
Space\Ziebro_Honors_Thesis\Thesis\off.mat')
load('C:\Users\ziebro.2\Dropbox\Interlab Shared
Space\Ziebro_Honors_Thesis\Thesis\offc.mat')
load('C:\Users\ziebro.2\Dropbox\Interlab Shared
Space\Ziebro_Honors_Thesis\Thesis\offpp.mat')
load('C:\Users\ziebro.2\Dropbox\Interlab Shared
Space\Ziebro_Honors_Thesis\Thesis\offpp+au.mat')
load('C:\Users\ziebro.2\Dropbox\Interlab Shared
Space\Ziebro_Honors_Thesis\Thesis\open.mat')
load('C:\Users\ziebro.2\Dropbox\Interlab Shared
Space\Ziebro_Honors_Thesis\Thesis\open1.mat')
load('C:\Users\ziebro.2\Dropbox\Interlab Shared
Space\Ziebro_Honors_Thesis\Thesis\pap300.mat')
load('C:\Users\ziebro.2\Dropbox\Interlab Shared
Space\Ziebro_Honors_Thesis\Thesis\pap500.mat')
load('C:\Users\ziebro.2\Dropbox\Interlab Shared
Space\Ziebro_Honors_Thesis\Thesis\pp.mat')
load('C:\Users\ziebro.2\Dropbox\Interlab Shared
Space\Ziebro_Honors_Thesis\Thesis\pp_au2.mat')
% load('C:\Users\ziebro.2\Dropbox\Interlab Shared
Space\Ziebro_Honors_Thesis\Thesis\pp+au2.mat')

%figure
%plot(off.X.Data,off.Y.Data)

%figure
%plot(open.X.Data,open.Y.Data)

b=20;

G=39854.23/10000; %Multiplying by sensitivity and accounting for op amp gain
%% Part 0: Is there some offset pressure from the transducer?

offt=off.X.Data;
offp=-off.Y.Data*G; %Gain=1 + 50(kohm)/R, R=2 (ohm), %Sensitivity= 996.36
Pa/0.025V

ot=open.X.Data;
op=-open.Y.Data*G;
d(1:length(op),1)=op;
```

```
%Or, 0.14451 psi / 0.025 V = 5.78036 psi/V

fsize=12;
n=1;

A=[0 10 -2 3];

% figure(n)
% set(n,'Position',[10 650 600 450])
% plot(offt,offp, 'Linewidth',2)
% title('Fan Off, Pressure Should Be Close to Zero')
% xlabel('Time [sec.]')
% ylabel('Pressure [Pa]')
% axis(A)
% n=n+1;
% set(gca,'FontSize',fsize);
offset=mean(op);
sof=std(op);
figure(n)
histfit(op,b);
n=n+1;

%
% figure(n)
% set(n,'Position',[650 650 600 450])
% plot(offt,offp-offset,'Linewidth',2)
% title('Fan Off, Avg. Pressure is Zero')
% xlabel('Time [sec.]')
% ylabel('Pressure [Pa]')
% n=n+1;
% set(gca,'FontSize',fsize);
% axis(A)

%% Part 1: Completely stop up the exit. Pmax

clt=closed2.X.Data;
clp=-closed2.Y.Data*G-offset;
d(1:length(op),2)=clp;


% figure(n)
% set(n,'Position',[1300 650 600 450])
% plot(clt,clp)
% title('Closed Manifold')
% xlabel('Time [sec.]')
% ylabel('Pressure [Pa]')
% axis(A)
% n=n+1;
% set(gca,'FontSize',fsize);
pmax=mean(clp);
smax=std(clp);
offset=mean(op);
sof=std(clp);
figure(n)
```

```
histfit(clp,b);
n=n+1;

%% Part 2: Carbon Substrate

ct=c.X.Data;
cp=-c.Y.Data*G-offset;
d(1:length(op),3)=cp;


% figure(n)
% set(n,'Position',[10 50 600 450])
% plot(ct,cp)
% title('Carbon Substrate Manifold Pressure vs. Time')
% xlabel('Time [sec.]')
% ylabel('Pressure [Pa]')
% axis(A)
% n=n+1;
% set(gca,'FontSize',fsize);
pcarbon=mean(cp);
scarbon=std(cp);
figure(n)
histfit(cp,b);
n=n+1;

%% Part 3: Polypropylene

ppt=pp.X.Data;
ppp=-(pp.Y.Data)*G-offset;
d(1:length(op),4)=ppp;

% figure(n)
% set(n,'Position',[650 50 600 450])
% plot(ppt,ppp)
% title('Polypropylene')
% xlabel('Time [sec.]')
% ylabel('Pressure [Pa]')
% axis(A)
% n=n+1;
% set(gca,'FontSize',fsize);
ppoly=mean(ppp);
spoly=std(ppp);
figure(n)
histfit(ppp,b);
n=n+1;

%% Part 4: PP + Gold

ppaut=ppt;
ppaup=-(pp_au2.Y.Data)*G-offset;
d(1:length(op),5)=ppaup;

% figure(n)
% set(n,'Position',[1300 50 600 450])
% plot(ppaut,ppaup)
```

```
% title('Polypropylene + Gold')
% xlabel('Time [sec.]')
% ylabel('Pressure [Pa]')
% axis(A)
% n=n+1;
% set(gca,'FontSize',fsize);
pppau=mean(ppaup);
sppau=std(ppaup);
figure(n)
histfit(ppaup,b);
n=n+1;

%% Part 5: PP + Gold + PPy

p3t=pap300.X.Data;
p3p=-pap300.Y.Data*G-offset;
d(1:length(op),6)=p3p;

% figure(n)
% set(n,'Position',[1300 50 600 450])
% plot(ppaut,ppaup)
% title('Polypropylene + Gold + Polypyrrole')
% xlabel('Time [sec.]')
% ylabel('Pressure [Pa]')
% axis(A)
% n=n+1;
% set(gca,'FontSize',fsize);
ppap300=mean(p3p);
spap300=std(p3p);
figure(n)
histfit(p3p,b);
xlabel('Pressure [Pa]')
ylabel('Number of Occurrences')
title('Pressure Data Histogram')
set(gca,'FontSize',fsize)
n=n+1;

%% Part 6: All on Same Plot

figure(n)
plot(clt,clp,p3t,p3p,ppaut,ppaup,ppt,ppp,ct,cp)
%ppt,ppp,ppaut,ppaup,p3t,p3p,clt,clp)
set(n,'Position',[2000 650 600 450])
set(gca,'FontSize',fsize);
title('Comparison of Manifold Pressures of Membranes')
xlabel('Time [sec.]')
ylabel('Pressure [Pa]')
legend('Closed','PP+Au+PPy','PP+Au','PP','Carbon')
n=n+1;

% figure(n)
% n=n+1;
% a=[1 1];
% b=[1 1];
% X=clp;
% Y=filter(b,a,X)
```

```
% plot(clt,Y)


%% Part 7: Calculations

A1=(pi)/4*(2*.0254)^2; %m^2
A2=(pi)/4*(0.25*.0254)^2; %m^2
rho=1.2; %kg/m^3

p(1)=pcarbon;
p(2)=ppoly;
p(3)=pppau;
p(4)=ppap300;

s(1)=scarbon;
s(2)=spoly;
s(3)=sppau;
s(4)=spap300;

x=min(op):0.01:max(pmax);
y=95*ones(length(x));

for n=1:4
    v(n)=sqrt(2*(pmax-p(n))/rho);
    q(n)=v(n)*A2;
    R(n)=p(n)./q(n);
    dist(1:length(x),n)=normcdf(x,p(n),s(n));
    z(n)=icdf('Normal',0.95,p(n),s(n));
    figure
    plot(x,100*dist(1:length(x),n))
    CI(1,n)=p(n)-z(n).*s(n)/sqrt(length(op));
    CI(2,n)=p(n)+z(n).*s(n)/sqrt(length(op));
    set(gca,'FontSize',fsize)
    xlabel('Pressure [Pa]')
    ylabel('Probability [%]')
    title('Cumulative Density Function')
end

%Units are Pa*s/m^3
```

Appendix C: Instrument Specification Sheets

MINIATURE SILICON PRESSURE SENSORS
TEMPERATURE COMPENSATED

NEW

PRESSURE TRANSDUCERS B

Gage, Absolute or Differential Pressure
4 inH$_2$O to 150 psi
10 mbar to 10 bar

PXCPC Series

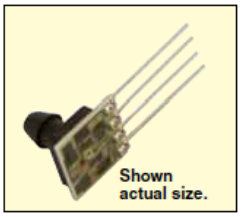

- Low Cost, Small Size, PC Board Mountable
- Micromachined Silicon Technology
- High Impedance, Low Current Draw
- 4-Pin Package
- For Use with Clean Dry Gases

The PXCPC Series pressure sensors come standard with tube pressure ports and use state-of-the-art micromachined silicon technology to deliver accurate, stable pressure measurement in a miniature package. On sensors of 5 psi and above the high side of the silicon is protected by a silicone gel coating. The sensors are designed for use with non-corrosive non-ionic gases. Many industrial and research gases fall into this category.

PXCPC

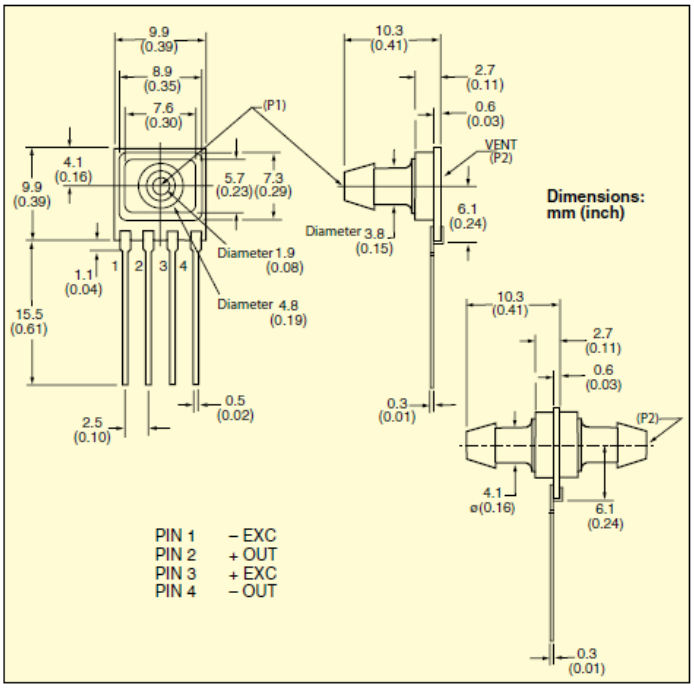

B-1

SPECIFICATIONS

@ 12 Vdc, 25°C (77°F)
Excitation: 12 Vdc typical (3 Vdc minimum to 16 Vdc maximum)
Output mV (@ 12 Vdc) Range:
4 inH$_2$O: 25 ±2 mV
10 inH$_2$O: 20 ±1 mV
1 psi: 18 ±1 mV
5 psi: 60 ±1 mV
15 to 60 psi: 90 ±5 mV
100 psi: 100 ±5 mV
150 psi: 90 ±5 mV
Linearity, Hysteresis Error: 0.25% typical 1% maximum
Operating Temperature: -25 to 85°C (-13 to 185°F)
Compensated Temperature: 0 to 70°C (32 to 158°F)
Thermal Effects
Zero Shift: ±1.0 mV
Span Shift: ±2.0% span
Input Impedance: 5 kΩ
Output Impedance: 3 kΩ
Over Pressure (Maximum)
Absolute: The lesser of 3 x full scale or 250 psi
Gage/Diff:
≤ 1 psi Range: 3 psi maximum
>1 psi: The lesser of 3 x full scale of 250 psi
Common Mode Pressure: 50 psi maximum
Weight: 2 g (0.06 oz)

Figure 21: Pressure transducer specification sheet

SPECIFICATIONS

ELECTRICAL

At T_A = +25°C, V_S = ±15V, R_L = 2kΩ, unless otherwise noted.

PARAMETER	CONDITIONS	INA114BP, BU			INA114AP, AU			UNITS
		MIN	TYP	MAX	MIN	TYP	MAX	
INPUT								
Offset Voltage, RTI								
Initial	T_A = +25°C		±10 + 20/G	±50 + 100/G		±25 + 30/G	±125 + 500/G	µV
vs Temperature	T_A = T_{MIN} to T_{MAX}		±0.1 + 0.5/G	±0.25 + 5/G		±0.25 + 5/G	±1 + 10/G	µV/°C
vs Power Supply	V_S = ±2.25V to ±18V		0.5 + 2/G	3 + 10/G		*	*	µV/V
Long-Term Stability			±0.2 + 0.5/G			*		µV/mo
Impedance, Differential			10^{10} || 6			*		Ω || pF
Common-Mode			10^{10} || 6			*		Ω || pF
Input Common-Mode Range		±11	±13.5		*	*		V
Safe Input Voltage				±40			*	V
Common-Mode Rejection	V_{CM} = ±10V, ΔR_S = 1kΩ							
	G = 1	80	96		75	90		dB
	G = 10	96	115		90	106		dB
	G = 100	110	120		106	110		dB
	G = 1000	115	120		106	110		dB
BIAS CURRENT			±0.5	±2		*	±5	nA
vs Temperature			±8			*		pA/°C
OFFSET CURRENT			±0.5	±2		*	±5	nA
vs Temperature			±8			*		pA/°C
NOISE VOLTAGE, RTI	G = 1000, R_S = 0Ω							
f = 10Hz			15			*		nV/√Hz
f = 100Hz			11			*		nV/√Hz
f = 1kHz			11			*		nV/√Hz
f_B = 0.1Hz to 10Hz			0.4			*		µVp-p
Noise Current								
f=10Hz			0.4			*		pA/√Hz
f=1kHz			0.2			*		pA/√Hz
f_B = 0.1Hz to 10Hz			18			*		pAp-p
GAIN								
Gain Equation			1 + (50kΩ/R_G)			*		V/V
Range of Gain		1		10000	*		*	V/V
Gain Error	G = 1		±0.01	±0.05		*	*	%
	G = 10		±0.02	±0.4		*	±0.5	%
	G = 100		±0.05	±0.5		*	±0.7	%
	G = 1000		±0.5	±1		*	±2	%
Gain vs Temperature	G = 1		±2	±10		*	±10	ppm/°C
50kΩ Resistance[1]			±25	±100		*	*	ppm/°C
Nonlinearity	G = 1		±0.0001	±0.001		*	±0.002	% of FSR
	G = 10		±0.0005	±0.002		*	±0.004	% of FSR
	G = 100		±0.0005	±0.002		*	±0.004	% of FSR
	G = 1000		±0.002	±0.01		*	±0.02	% of FSR
OUTPUT								
Voltage	I_O = 5mA, T_{MIN} to T_{MAX}	±13.5	±13.7		*	*		V
	V_S = ±11.4V, R_L = 2kΩ	±10	±10.5		*	*		V
	V_S = ±2.25V, R_L = 2kΩ	±1	±1.5		*	*		V
Load Capacitance Stability			1000			*		pF
Short Circuit Current			+20/–15			*		mA
FREQUENCY RESPONSE								
Bandwidth, –3dB	G = 1		1			*		MHz
	G = 10		100			*		kHz
	G = 100		10			*		kHz
	G = 1000		1			*		kHz
Slew Rate	V_O = ±10V, G = 10	0.3	0.6		*	*		V/µs
Settling Time, 0.01%	G = 1		18			*		µs
	G = 10		20			*		µs
	G = 100		120			*		µs
	G = 1000		1100			*		µs
Overload Recovery	50% Overdrive		20			*		µs
POWER SUPPLY								
Voltage Range		±2.25	±15	±18	*	*	*	V
Current	V_{IN} = 0V		±2.2	±3		*	*	mA
TEMPERATURE RANGE								
Specification		–40		85	*		*	°C
Operating		–40		125	*		*	°C
θ_{JA}			80			*		°C/W

Figure 22: Operational amplifier specification sheet

Technical Details

Parameter		Specification
Processor		■ MPC8240 processor with PPC 603e core and on-chip peripherals ■ 64-bit floating-point processor ■ CPU clock: 250 MHz ■ 2 x 16 KB cache, on-chip ■ On-chip PCI bridge (33 MHz)
Memory	Global memory	■ 32 MB SDRAM
	Flash memory	■ 8 MB
Timer	4 general-purpose timers	■ 32-bit down counter ■ Reload by hardware ■ 80-ns resolution
	1 sampling rate timer (decrementer)	■ 32-bit down counter ■ Reload by software ■ 40-ns resolution
	1 time base counter	■ 64-bit up counter ■ 40-ns resolution
Interrupt controller		■ 5 timer interrupts ■ 2 incremental encoder index line interrupts ■ 1 UART interrupt ■ 1 slave DSP interrupt ■ 1 slave DSP PWM interrupt ■ 5 A/D converter (end of conversion) interrupts ■ 1 host interrupt ■ 4 external interrupts (user interrupts)
A/D converter	Channels	■ 4 multiplexed channels equipped with one sample & hold A/D converter (1x16-bit) ■ 4 parallel channels each equipped with one sample & hold A/D converter (4x12-bit) ■ Note: 5 A/D converter channels (1x16-bit and 4x12-bit) can be sampled simultaneously
	Resolution	■ Multiplexed channels: 16 bit ■ Parallel channels: 12 bit
	Input voltage range	■ ±10 V
	Conversion time	■ Multiplexed channels: 2 µs[1)] ■ Parallel channels: 800 ns[1)]
	Offset error	■ ±5 mV
	Gain error	■ Multiplexed channels: ±0.25% ■ Parallel channels: ±0.5%
	Offset drift	■ 40 µV/K
	Gain drift	■ 25 ppm/K
	Signal-to-noise ratio	■ Multiplexed channels: >80 dB ■ Parallel channels: >65 dB
D/A converter	Channels	■ 8 channels
	Resolution	■ 16-bit
	Output range	■ ±10 V
	Settling time	■ Max. 10 µs (full-scale, accuracy ½ LSB)
	Offset error	■ ±1 mV
	Gain error	■ ±0.1%
	Offset drift	■ 130 µV/K
	Gain drift	■ 25 ppm/K
	Signal-to-noise ratio	■ >80 dB
	I_{max}	■ ±5 mA
Digital I/O	Channels	■ 20-bit parallel I/O ■ Single bit selectable for input or output
	Voltage range	■ TTL input/output levels
	$I_{out, max}$	■ ±5 mA

Figure 23: dSpace data acquisition specifications